Connecting the branches of multistable non-Euclidean origami by crease stretching

Clark C. Addis ⬤, Salvador Rojas ⬤, and Andres F. Arrieta ⬤*

Programmable Structures Lab, School of Mechanical Engineering, Purdue University, West Lafayette, Indiana 47907, USA

Non-Euclidean origami is a promising technique for designing multistable deployable structures folded from nonplanar developable surfaces. The impossibility of flat foldability inherent to non-Euclidean origami results in two disconnected solution branches each with the same angular deficiency but opposite handedness. We show that these regions can be connected via "crease stretching," wherein the creases exhibit extensibility in addition to torsional stiffness. We further reveal that crease stretching acts as an energy storage method capable of passive deployment and control. Specifically, we show that in a Miura-Ori system with a single stretchable crease, this is achieved via two unique, easy to realize, equilibrium folding pathways for a certain wide set of parameters. In particular, we demonstrate that this connection mostly preserves the stable states of the non-Euclidean system, while resulting in a third stable state enabled only by the interaction of crease torsion and stretching. Finally, we show that this simplified model can be used as an efficient and robust tool for inverse design of multistable origami based on closed-form predictions that yield the system parameters required to attain multiple, desired stable shapes. This facilitates the implementation of multistable origami for applications in architecture materials, robotics, and deployable structures.

I. INTRODUCTION

Origami is the ancient Japanese art of paper folding. The simple algebraic kinematics of origami-inspired systems gives rise to its characteristic reconfigurability, which has resulted in numerous applications in robotic locomotion [1–4], meta-material architecture [5], compact deployable structures such as bridges and stadium covers [6], reconfigurable wheels [7], and—notably—simple yet robust inverse shape design algorithms [8–11]. Classical origami assumes that shape change stems from folding of an infinitely thin surface involving no deformation or change in strain energy [12]. Consequently, engineering systems inspired by origami formalism theoretically behave as mechanisms, which by definition do not resist displacement along their degrees of freedom. However, physical embodiments of origami [13] do in fact show resistance to displacement, either due to torsional stiffness [14] or active elements used to achieve desired kinematic configurations [15]. The former typically shows a single stable shape, while the latter can achieve several configurations at the cost of complex actuation systems and control.

Engineers have investigated the potential of origami with multiple energetic minima, or multistable origami, to add load-bearing capacity and pathway configurability without the need for continuous actuation and complex control. One approach takes advantage of hidden degrees of freedom due to facet bending [16–19]. However, this excludes the utilization of functional materials such as semiconductors (e.g., photovoltaics or transistors) that cannot cope with the large facet strains experienced during bending.

On the contrary, a second approach assumes rigid facets while relying on elastic bending moments via crease torsion to produce multistability [20–22]. Waitukaitis *et al.* have shown that crease torsion alone can achieve up to five stable configurations for a four-faceted origami system [23]. However, two key drawbacks remain: (1) the folding paths have multiple solutions that overlap at the flat state [24], and (2) inverse design is difficult due to the coexisting solutions (pathway degeneracy) and the complex multidimensional problem of fine-tuning the crease stiffness to match a desired state [25–27].

Non-Euclidean origami shows promise to address some of these challenges. This class of origami is still folded from developable, zero Gaussian curvature sheets, but instead of subtending an angle of 2π about a particular vertex, as is the case for traditional origami [Fig. 1(a)(i)], it is folded from some angular deficiency of less than 2π (a cone [28,29]) or some angular excess of greater than 2π [an E-cone [30], Fig. 1(a)(ii)]. Non-Euclidean origami circumvents the pathway degeneracy of traditional origami because it always results in two separate folding regimes when folded from a cone, no matter how many creases are added [28,31]. Intuitively, this is because the two regions represent two mirrored cones [Figs. 1(a)(iii), 1(a)(iv), and 1(b)]. The kinematics of non-Euclidean origami preserve the ability to be described by simple algebraic equations [32–34] and, in many instances, has succeeded in passively preventing misfolding [29,35,36]. This comes at the cost of effectively halving the possible design space.

Resilin, a multipurpose biopolymer commonly found in insect wings [37–40] serves as an inspiration to expand this design space while enabling multistability. Resilin assigns mountain or valley folds to origamilike insect wings [41,42] and serves as an energy storage device, for example, in the

─────────
*aarrieta@purdue.edu

(a)

(i) $\beta = 0$

Plane

(ii) $\beta < 0$

e-Cone

(iii) $\beta > 0$

Cone 1

(iv) $\beta > 0$

Cone 2

(b)

(i)

ρ_3 φ
α
ρ_2 ρ_4
ρ_1 α

Folded From Cone 1

$\varphi_{I,1}(\alpha)$

(ii)

ρ_4 φ
α
ρ_1 α ρ_3
ρ_2

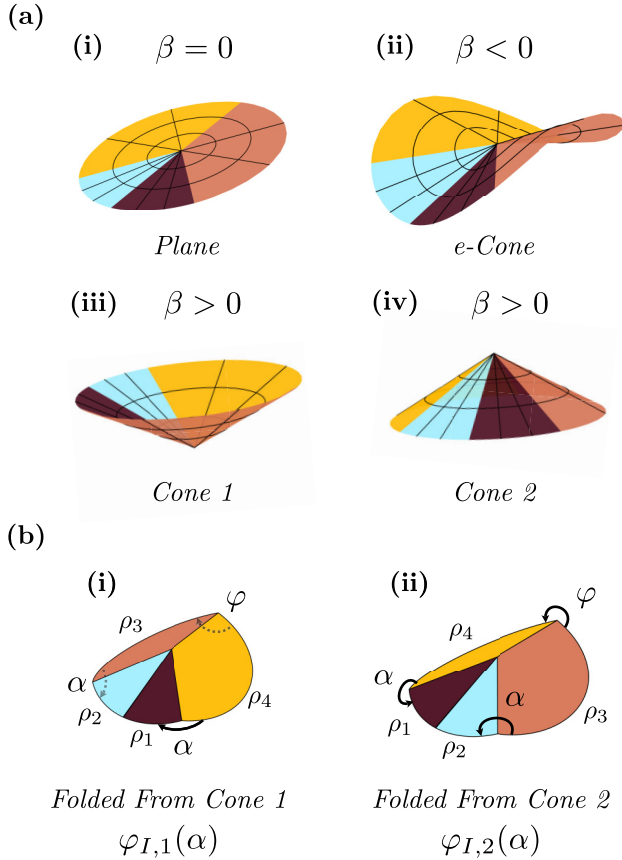*Folded From Cone 2*

$\varphi_{I,2}(\alpha)$

FIG. 1. (a) Origami can be folded from different surfaces of varied angular deficiency (β). (i) When $\beta < 0$, we have angular excess, and an e-Cone is observed. (ii) When $\beta = 0$, we are folding from a flat plane (traditional origami). (iii) When $\beta > 0$, we are folding from a cone. (iv) There always exists another unique cone with the same $\beta > 0$. (b) The two mirrored cones create two disconnected kinematically admissible pathways. (i) The first pathway's facets are ordered clockwise as ρ_i increases ($\rho_1 \rightarrow \rho_2 \rightarrow \rho_3 \rightarrow \rho_4$) and are folded from cone 1, named $\varphi_{I,1}$. (ii) The second pathway's facets are ordered counter-clockwise as ρ_i increases, and are folded from cone 2, named $\varphi_{I,2}$.

Rove Beetle [43] and the Earwig [44]. However, the Earwig wing is unique in that the energy is stored via stretching in the creases in addition to crease torsion. This crease stretching or "spring origami" has been shown to explain the bistability and curved creases displayed by the Earwig wing [45], opening up a vast design space for origami-based systems that localize all flexibility to the folds.

In this paper, we show that crease stretching can connect the oppositely-handed folding regimes of non-Euclidean origami without relying on facet deformation, while retaining the benefit of simple pathway control and straightforward inverse design. This is achieved by establishing a tractable analytical method applied to the well-known Miura-Ori unit. We begin with the Miura-Ori folded from the two possible non-Euclidean cones, then relax the rigid crease assumption of classical origami by allowing them to stretch while maintaining infinite facet rigidity. By folding the manifold representing the kinematic space into the energetic space, we can show that inherent symmetries directly predict the existence of a

minimum of two, and usually three stable configurations. Furthermore, through derivation of the folding paths, our model allows us to show that crease stretching does not add degeneracy. The analytically predicted configurations and folding paths accurately match benchtop experiments. Our results show that the stable states from the purely non-Euclidean approach are mostly preserved, while adding a third. Finally, we show how the model is simple enough to be used in inverse design calculations, yet robust enough to be confirmed by experiments.

II. ALTERNATIVE MODELS FOR CREASE STRETCHING

We begin with a discussion of alternative models of flexible creases in origami. For sufficiently thin sheets, a straightforward approach is to neglect the effect of stretching, and to assume that the energetics of crease bending are dominated by torsional deformations. Models based on symmetric Elastica curves make use of rotational springs at curve intersection [46–49], while others ignore the bulk and focus on a single nonlinear [50,51] or linear [52–56] spring whose constants are based on material models. However, we cannot discount crease extensibility during bending because (1) we employ thick creases in this work as thin creases are difficult to manufacture using fused deposition modeling (FDM) 3D printing and (2) we know that kinematically the angular material must be able to stretch to accommodate the transition between non-Euclidean cones. A second approach is to create beamlike models which has been achieved using finite element methods [57–59], or hyperelastic material models [60]. While highly descriptive and accurate, these beamlike models are computationally expensive and difficult to perform inverse on.

The F-cone model which entails a cone with at least one fold in it [61] is the closest analytical model that can account for both torsion and stretching. Notably, F-cones remains bistable, even when part of the central fold is removed [62], a fact that we leverage in our experiments. Nevertheless, the deformation process is still rather complex to model, requiring numerical approximations [63], which makes this approach cumbersome for inverse design.

"Spring origami" offers a computationally simple yet powerful model where the crease is represented by a combination of a rotational and extensional spring [45]. Rojas *et al.* have used it to model 3D printable multistable grippers [64] and the reconfiguration of temperature sensitive shape memory polymers [65]. Due to its ability to capture both the torsion and stretching of a system with the minimum possible complexity, we choose to use "spring origami" throughout this work.

III. PROBLEM DEFINITION

Non-Euclidean origami refers to a 2D surface with sector angles ρ_i subtending an angle of $2\pi + \epsilon$ about the vertex [29], where ϵ is the angular excess. Equivalently, the surface can be folded from sectors with a subtending angle of $2\pi - \beta$ [45], where β is the angular deficit. In general, $\beta = -\epsilon$, and we will use β throughout, since pathway disconnection occurs only in systems with angular deficit [28]. We choose to examine a Miura-Ori unit, an origami fold pattern originally developed

(a)

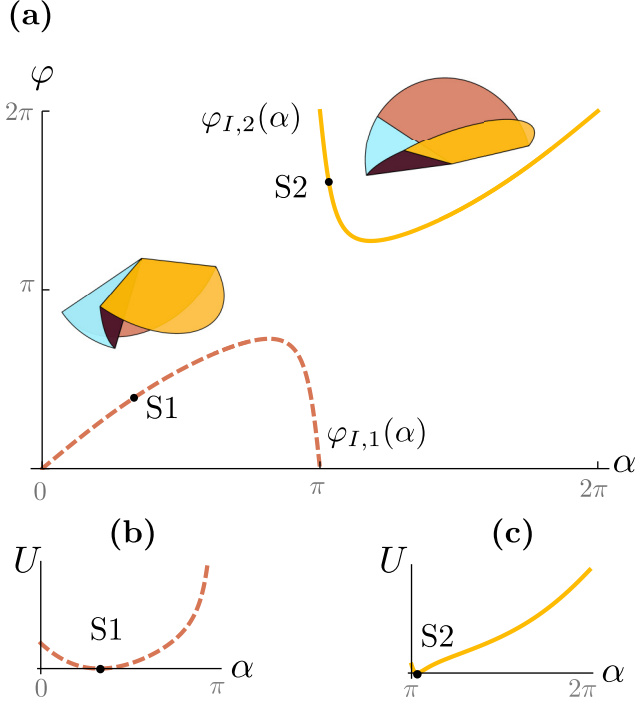**(b)**   **(c)**

FIG. 2. (a) Non-Euclidean origami with an angular deficiency has two disconnected pathways, each represented by an oppositely handed cone. When a rotational spring is added, two disconnected stable states form. (b) The energy landscape for path/cone 1 and stable state/local minimum S1. (c) The energy landscape for path/cone 2 and stable state/local minimum S2.

for folding membranes in space mechanisms [66], given the extensive attention it has received in the literature and its universal applications. For a symmetric Miura-Ori unit, one additional geometric parameter γ [5] is required to define the symmetric facets $\rho_1 = \rho_4$ [shown in Fig. 2(a)(i)]. Using spherical trigonometry techniques (developed in Ref. [67]) for the basic case of a non-Euclidean system without crease stretching we can write the kinematics (see derivation details in Supplemental Material (SM) A.3.5 [68]) as

$$\varphi_{I,n}(\alpha) = 2\tan^{-1}\left[\frac{\sin\alpha}{-\cot(\gamma+\beta/2)\sin\gamma - \cos\gamma\cos\alpha}\right]$$
$$+ 2\pi(n-1), \tag{1}$$

with $n = 1$ or $n = 2$, where φ and α are the dihedral angles defined in Fig. 4(a). Notice, that Eq. (1) results in two folding pathways: $\varphi_{I,1}(\alpha)$ (left) and $\varphi_{I,2}(\alpha)$ (right), plotted in Fig. 2(a) as Eq. (1) with $\gamma = 3\pi/4$ and $\beta = 10°$. This matches prior work establishing that for $\beta > 0$ two disconnected pathways always exist [28]. The disconnected pathways can be abstracted as two "oppositely handed" cones. For path 1, when viewed with the vertex at the top, ρ_i cyclically increases in the clockwise direction around the directrix [Fig. 2(a)(i)], whereas for path 2, ρ_i cyclically increases in the counterclockwise direction around the directrix [Fig. 2(a)(ii)].

We consider the addition of a rotational spring between facets ρ_2 and ρ_3, with an equilibrium angle $\theta_0 = 79.76°$ which reveals two stable states S1 and S2. The equilibrium angle $\alpha_{0,1}$
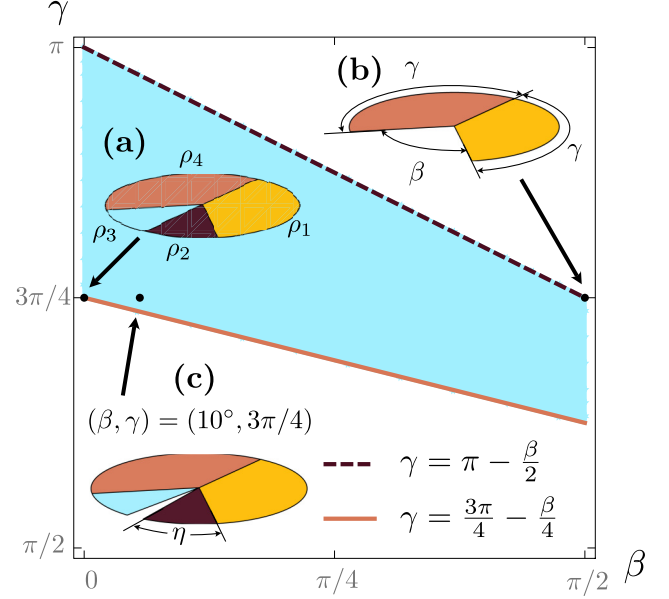

FIG. 3. The valid parameter space for this analysis is highlighted by the shaded area. There are two boundaries: the upper boundary corresponds to $\eta = 0$, and the lower boundary simplifies the kinematic analysis. The point at $\beta = 10°$ and $\gamma = \frac{3\pi}{4}$ is used throughout this study.

for stable state S1 on pathway 1 can be calculated using

$$\alpha_{0,1} = \cos^{-1}\left[\frac{\cot\gamma\sin\eta}{\sqrt{\cos^2\eta + \cot^2(\theta_0/2)}}\right]$$
$$- \tan^{-1}\left[\frac{\cot(\theta_0/2)}{\cos\eta}\right], \tag{2}$$

and the equilibrium angle $\alpha_{0,2}$ for stable state S2 on pathway 2 can be calculated as

$$\alpha_{0,2} = 2\pi - \cos^{-1}\left[\frac{\cot\gamma\sin\eta}{\sqrt{\cos^2\eta + \cot^2(\theta_0/2)}}\right]$$
$$- \tan^{-1}\left[\frac{\cot(\theta_0/2)}{\cos\eta}\right]. \tag{3}$$

Equations (2) and (3) are derived by using spherical trigonometry and the harmonic identity to locate the coordinates where the gradient of the energy is zero as detailed in SM B.3 [68]. Notice, however, that in Figs. 2(b) and 2(c) the two stable states lie on two different pathways. Thus, these two stable states could never be physically realized on the same rigid system. These disconnected pathways (i.e., disjointed sets) are an intrinsic characteristic of n-fold, non-Euclidean origami with an angular deficiency [28]. In the following, we establish a method to connect these disjointed regions in a physical system while retaining bistability by allowing crease stretching.

IV. PARAMETER SPACE

We first define the derived parameter η, which is equivalently the facet angle subtending ρ_2, and the facet angle subtending ρ_3 [Fig. 3(a)]. We define that in the flat state, η,
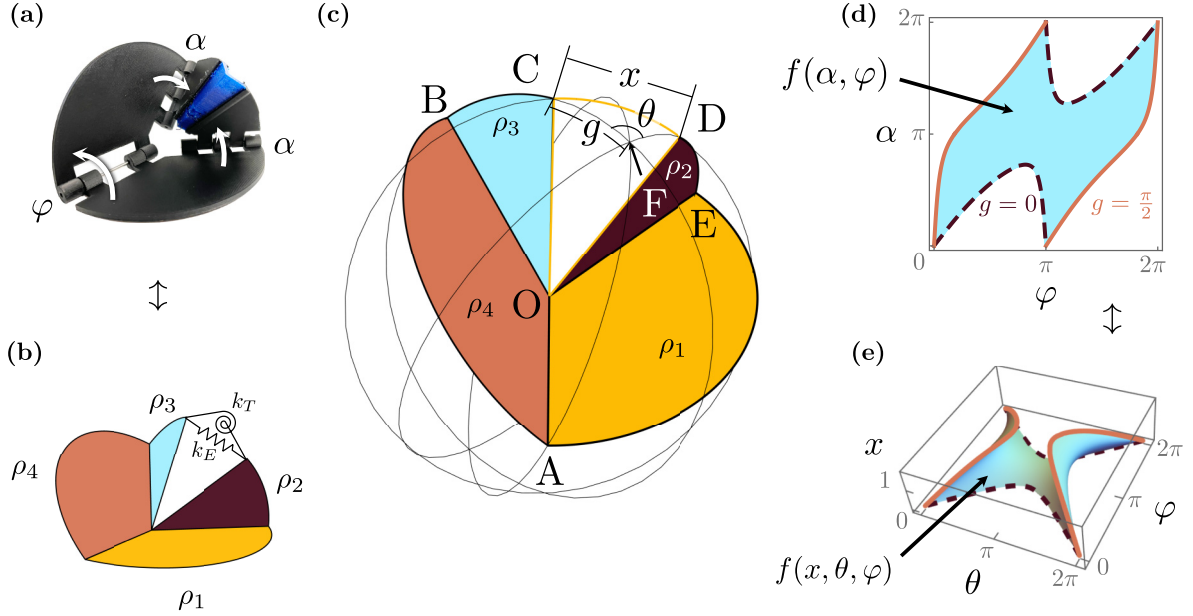
FIG. 4. (a) We treat the stretchable crease as a torsional and extensional spring with stiffness k_T and k_E. (b) The 2 degrees of freedom, φ and α, completely define the kinematic space. (c) If all of the dihedral edges are unit length, then all endpoints lie on a sphere. The spring k_E acts over distance x, which is the chord from point C to point D, and the spring k_T acts about angle θ which is the angle defined by $\triangle CFD$ about point F. The parameter g is useful in establishing the kinematic bounds, and it is equal to arc $FC = FD$. (d) Not all φ-α pairs are valid. When $g = 0$ the facets intersect, and when $g = \pi/2$ the extensional spring clips through the facets, both of which are physically impossible. (e) We can fold the α-φ kinematic space into x-θ-φ space to simplify the energetic analysis.

γ, and β lie in a plane [see Fig. 3(b) for definition of γ and β and Fig. 3(c) for definition of η]. Thus, they are explicitly related by

$$2\eta + 2\gamma + \beta = 2\pi. \tag{4}$$

We introduce parametric bounds on our system, by first enforcing that $\eta > 0$, implying that facets ρ_2 and ρ_3 will always exist. Using Eq. (4), this definition is equivalent to the statement

$$\gamma < \pi - \beta/2. \tag{5}$$

To allow for the space folding technique employed in Sec. VI, we impose that the kinematic space always form a closed region using the two kinematic boundaries we establish in Sec. V (see SM A.4.1 [68] for details) resulting in the additional restriction that

$$\gamma > 3\pi/4 - \beta/4. \tag{6}$$

Finally, to further simplify our analysis (see SM A.3.3 [68] for full justification), we restrict β and γ to the domains

$$0 < \beta < \pi/2 \quad \text{and} \quad \pi/2 < \gamma < \pi. \tag{7}$$

The four constraints given by Eqs. (5)–(7) form a closed region represented by the shaded area in Fig. 3. The geometric parameters used throughout this article are $\beta = 10°$ and $\gamma = 3\pi/4$ [Fig. 3(c)].

V. KINEMATICS AND ENERGETICS

The kinematic analysis of a stretchable crease unit requires the definition of two independent degrees of freedom φ and α [Fig. 4(a)]. This effectively creates a cut at ρ_2 and ρ_3. Allowing φ and α to both be members of the open set $(0, 2\pi)$ provides all possible configurations of the system.

To represent a flexible crease [the material between ρ_2 and ρ_3 in Fig. 4(a)], we use a rotational spring of stiffness k_T with equilibrium angle θ_0 and an extensional spring of stiffness k_E with equilibrium distance x_0 [Fig. 4(b)], which act on θ and x, respectively [Fig. 4(c)]. We define θ to be the angle subtended by the spherical arc CD from point F, while we define x as the Euclidean distance between points C and D. Finally, we assume the restoring force from the stretchable crease to be of a significantly higher order of magnitude than the potential due to gravity allowing us to ignore the effect of mass in the facets (ρ_i). We further assume quasistatic loading which implies symmetric bending moments on points C and D [Fig. 4(c)], and effectively excludes asymmetric folding modes. The resulting energetics are captured by

$$U = \tfrac{1}{2}(k_E[x(\alpha, \varphi) - x_0]^2 + k_T[\theta(\alpha, \varphi) - \theta_0]^2). \tag{8}$$

Interestingly, assuming rigid facets and lumped springs impose two kinematic constraints on the system. These two constraints can be described by the parameter $g = FC = FD$ [Fig. 4(c)]. The first constraint is that facets ρ_2 and ρ_3 cannot intersect, corresponding to $x = 0$, or $g = 0$ in Fig. 4(d). Equivalently, this boundary is the kinematic space of a non-Euclidean system without crease stretching, and thus

is directly defined by Eq. (1). We refer to this as the "intersect boundary," φ_I. The second constraint is $g = \pi/2$, which corresponds to when facets ρ_2 and ρ_3 are parallel to each other, rendering impossible the placement of a rotational spring. We refer to this as φ_S, for "spring boundary," and it is defined by (see SM A.3.4 [68] for this derivation)

$$\varphi_S(\alpha) = \pi - 2\tan^{-1}\left(\frac{\tan(\gamma + \beta/2)\sin\gamma - \cos\gamma\cos\alpha}{\sin\alpha}\right). \tag{9}$$

We plot Eqs. (1) and (9) in α-φ space [Fig. 4(d)] and show that they always form a closed region, given the parameter limits outlined in Fig. 3 (see SM A.4 [68] for details).

VI. STABILITY ANALYSIS

Transforming the kinematics from α-φ to x-θ coordinates simplifies the stability analysis because the energetics of the problem, as defined in Eq. (8), are in x and θ. However, x-θ coordinates do not provide a one-to-one mapping to α-φ coordinates as described in SM A.5 [68]. This motivates our choices to use x-θ-φ coordinates to represent the system, which effectively folds α-φ space into three dimensions, as shown in Fig. 4(e), and provides a one-to-one mapping to α-φ space. To characterize this surface, we can write a level curve $f(x, \theta, \varphi) = 0$, using the spherical law of sines, as detailed in SM A.7 [68], yielding

$$f(x, \theta, \varphi) = \frac{\sin(\theta/2)}{\sin\gamma} - \frac{\sin(\varphi/2)}{\sin\left(\eta + \sin^{-1}\left[\frac{x}{2\sin(\theta/2)}\right]\right)} = 0. \tag{10}$$

Prior work has established that energy minima, and thus stable states, occur when the gradient of energy (∇U) and the gradient of the kinematic space (∇f) point in the same direction [69]. Using the dot product, this statement can be equivalently written as

$$\nabla U \cdot \nabla f = |\nabla U||\nabla f|, \tag{11}$$

where the gradient operator is defined in x-θ-φ coordinates. Applying this definition of the gradient to Eqs. (8) and (10) yields ∇U and ∇f as

$$\nabla U = [k_E(x - x_0), k_T(\theta - \theta_0), 0] \tag{12}$$

and

$$\nabla f = \left[\frac{\partial f}{\partial x}, \frac{\partial f}{\partial \theta}, \frac{\partial f}{\partial \varphi}\right]. \tag{13}$$

Notice that Eq. (12) establishes that the energy gradient is always a 2D vector, and Eq. (13) reveals that kinematic gradient is, in general, a 3D vector. Therefore, the two vectors point in the same direction only when the kinematic vector degenerates into a 2D vector in the x-θ plane. Inspection of Eq. (13) reveals that this collapse occurs when $\partial f/\partial\varphi = 0$. Our analysis in SM B.1.2 [68] shows that $\partial f/\partial\varphi = 0$ occurs when $\varphi = \pi$. We can visually establish in Fig. 5(a) that this stable state (T3) indeed occurs within the plane $\varphi = \pi$ in x-θ-φ space, and in Fig. 5(b) on the line $\varphi = \pi$ in α-φ space.

To uncover the other stable states, we reexamine Eq. (11) and determine that $\nabla f = 0$ or $\nabla U = 0$ also satisfy this expression. We show in SM B.1.3 [68] that ∇f is never zero and from inspection of Eq. (12) we observe that is $\nabla U = 0$ when
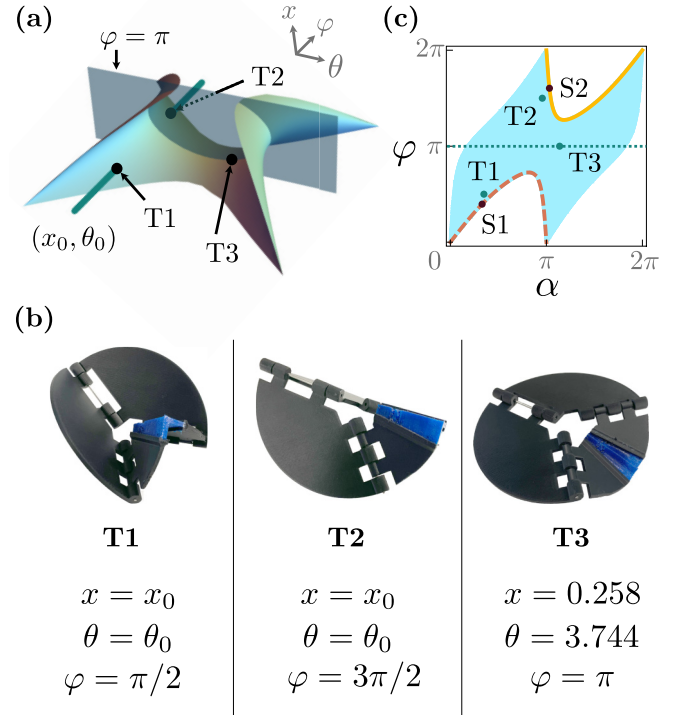

FIG. 5. (a) Our model predicts three stable states, two of which result from the global minima (T1, T2) and one of which is a local minimum of the balance of crease torsion and stretching (T3). We can prove mathematically that T3 only occurs along the plane $\varphi = \pi$, and that T1 and T2 occur twice along the line $x = x_0, \theta = \theta_0$. (b) This model is verified experimentally by setting our demonstrator to states T1, T2, and T3. (c) We compare the non-Euclidean case without crease stretching from Fig. 2 (dashed line being $\varphi_{I,1}$, solid line being $\varphi_{I,2}$, S1 being the stable state along $\varphi_{I,1}$, and S2 being the stable state along $\varphi_{I,2}$) to the non-Euclidean case with crease stretching. We note that S1 and S2 become T1 and T2, and a third state emerges, T3 at the dotted line $\varphi = \pi$.

$x = x_0$ and $\theta = \theta_0$. We reveal in SM A.5 [68] that this occurs exactly twice. To give a sense of this proof, we begin with the fact that Fig. 4(d) represents the complete kinematic space of the Miura-Ori system, with α and φ as our two degrees of freedom. Using Napier's analogies, we show that within this closed region, the inverse sine function produces two valid α-φ pairs for every pair of x_0 and θ_0, with the notable exception of x_0 and θ_0 values which produce a stable state at $\varphi = \pi$, i.e., the flat folded configuration. Figure 5(a) provides a visual intuition for why this is true: the solid line, which represents a given (x_0, θ_0), intersects the surface f twice (recall that the surface f is φ-α space folded into x-θ space), at T1 and T2, and is symmetric about $\varphi = \pi$. This method used to obtain (α_1, φ_1) and (α_2, φ_2) for T1 and T2, respectively, in SM A.5 [68] yields the following conditions:

$$\varphi_1 = 2\sin^{-1}\left[\frac{\sin\frac{\theta_0}{2}}{\sin\gamma}\sin\left(\eta + \sin^{-1}\left[\frac{x_0}{2\sin\frac{\theta_0}{2}}\right]\right)\right], \tag{14}$$

and

$$\varphi_2 = 2\pi - \varphi_1, \tag{15}$$

TABLE I. Degrees of freedom values and stability conditions predicted by our model for the three stable states for a system with parameters $\gamma = 3\pi/4$, $\beta = 10°$, $x_0 = 0.25$, $\theta_0 = 1.39$, and $k_E/k_T = 10^3$.

State	x	θ	α	φ	$\nabla U, \nabla f$
T1	0.250	1.39	1.10	$\pi/2$	$\nabla U = 0$
T2	0.250	1.39	3.01	$3\pi/2$	$\nabla U = 0$
T3	0.258	3.74	3.57	π	$\nabla U/|\nabla U| = \nabla f/|\nabla f|$

with

$$\alpha_{1,2} = 2\tan^{-1}\left[-\frac{\cos\left(\frac{1}{2}[\gamma \pm \eta]\right)}{\cos\left(\frac{1}{2}[\gamma \mp \eta]\right)}\tan\left(\frac{\varphi_1}{4} - \frac{\theta_0}{4}\right)\right]. \quad (16)$$

To obtain state T3, we write U as a function of α, holding φ constant at π and setting $\partial U/\partial\alpha = 0$ (SM B.2 [68]). Note that this requires choosing a ratio of k_E/k_T. We chose 10^3 because it is close to the range considered in Ref. [45] for which the predictions obtained with our model reveal the parameter values for the three stable states, as summarized in Table I.

The predicted parameter values by our closed-form solutions enable the design of the experimental demonstrator, shown in Fig. 5(b). In this demonstrator, we observe the symmetry of states T1 and T2 about $\varphi = \pi$ which have identical (x, θ) values. Additionally, the third stable state (T3), is found at $\varphi = \pi$. These experimental observations match closely the theoretical model predictions in Table I.

We now compare the stable states found by strict non-Euclidean origami [Fig. 2(a)] to the stable states for an equivalent system with the addition of crease stretching [Fig. 5(c)]. Note that the shaded region in Fig. 5(c) represents the kinematic space for crease stretching whereas the solid lines represents the kinematic space of strict non-Euclidean origami. Without crease stretching, we observe two disconnected stable states, S1 and S2. In contrast, allowing the crease to stretch connects the states via the shaded region (T1 and T2) and introduces an additional, kinematically accessible, third stable state (T3). Consequently, crease stretching connects the otherwise disjointed two stable states, i.e., S1 and S2.

VII. FOLDING PATHWAYS

Figure 5(b) showed that the three stable states have no kinematic obstacles between them. Here, we elucidate the two equilibrium folding pathways by which these states are connected using the principle of virtual work (SM C [68]). This approach reveals that there are two possible equilibrium pathways, one for each degree of freedom. One pathway corresponds to $\frac{\partial U}{\partial\alpha} = 0$. A solution to this equation fixes points O and A and applies two vertical downward forces, F_φ, at B and E [Fig. 6(a)(i)]. We define this to be the φ path because φ is our degree of freedom. The energy along this pathway is shown in Fig. 6(b). Notice that the endpoints of this path are T1 and T2, the two stable states established earlier. The other path corresponds to $\frac{\partial U}{\partial\varphi} = 0$. This pathway requires fixing points O, A, B, and E, and applying two vertical forces F_α at C and
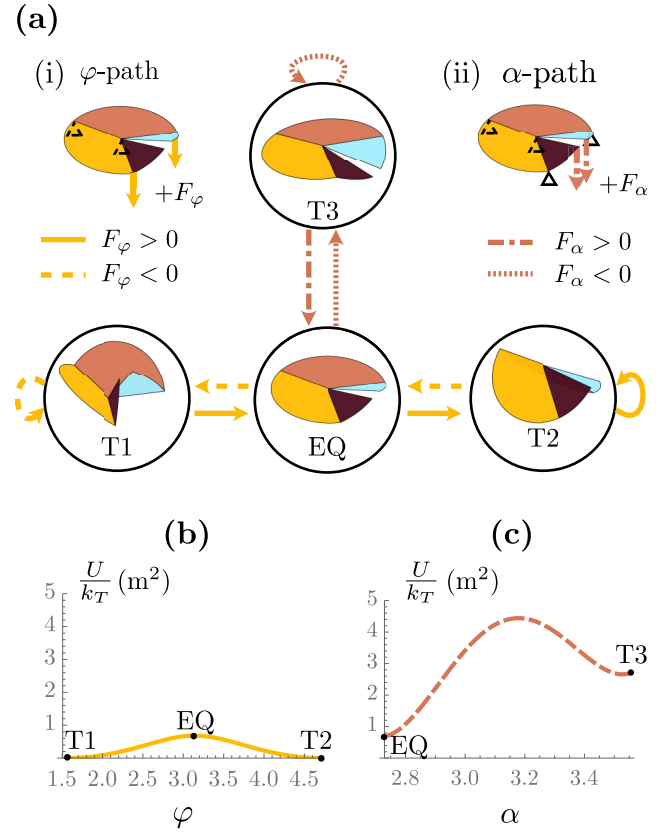

FIG. 6. (a) Stable states T1, T2, and T3 are connected by two main pathways (i) the φ path where φ is the only DOF, where when a $+F_\varphi$ is applied results in system folding from T1 to EQ and EQ to T2, and (ii) the α path where α is the only DOF, which when a positive F_α is applied results in folding from EQ to T3. (b) Energy landscape along the φ path, showing local maximum at EQ and local minima at T1 and T2. (c) The energy landscape along the α path, showing local minima at EQ and T3.

D, see Fig. 4(c) for the definition of points A-E and O. We define this to be the α path [Fig. 6(a)(ii)] because α is our degree of freedom. The energy along this pathway is shown in Fig. 6(c). The full energy landscape for the entire kinematic space is shown in Fig. 7(a).

Notice that in Fig. 6(c), state T3 is not connected directly to states T1 or T2. Instead, its endpoint is an intermediate saddle point EQ. Figure 6(a) summarizes how T1, T2, T3, and EQ are connected by the α path and the φ path. For instance, if we desire to move from state T1 to state T2, then we would apply a positive F_φ to the system with the boundary conditions of the φ path. Application of a positive F_φ past state T2, results in deflection back to state S2 upon release (see video S1). Figure 6(a) also indicates that to access state T3 from T1 requires the application of a positive F_φ under the boundary conditions of the φ path until the system is at the saddle point, EQ. Then, by switching a positive F_α with the boundary conditions of the α pathway, the system reaches state T3. Continuing to apply a positive F_α and subsequent release results in self-equilibrating deflection into state T3 (see video S2). For a given transition from one state to another, Fig. 6(c) can be read by starting at the initial state,
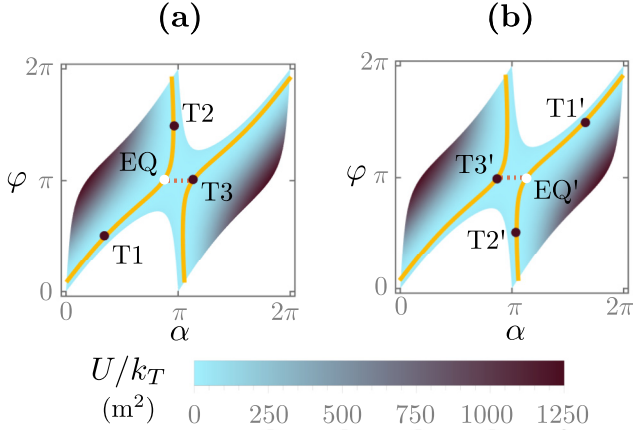
FIG. 7. Folding pathways, resulting stable states, and normalized strain energy choosing $\varphi_{0,1}$ (value of φ at T1) and x_0 as design objectives and θ_0 as our design variable. (a) For the design objective of $\varphi_{0,1} = \pi/2$ and $x_0 = 0.25$ inverse design results in $\theta_0 = 1.39$. (b) The same design objective is also achieved using $\theta_0 = 2\pi - 1.39$. By choosing (a) or (b), we can control whether the two stable states have α values in the open interval: (a) $(0, \pi)$ or (b) $(\pi, 2\pi)$.

and then applying $\pm F_\alpha$ or $\pm F_\varphi$ until the desired final state is reached.

VIII. INVERSE DESIGN

We now shift to the ultimate focus of this paper: to inversely design a spring origami Miura-Ori unit. We begin with a justification of our choice of design objective. Since there are a small number of elastomeric materials available for our manufacturing process (FDM 3D printing), we relate k_E and k_T at a ratio of $k_E/k_T = 10^3$, as before, and keep it fixed. We have also shown that choosing the shape of either T1 or T2 [$(\varphi_{T1}, \alpha_{T1})$ or $(\varphi_{T2}, \alpha_{T2})$] implies defining the other state's shape given their 2π symmetry in φ [see Eqs. (15) and (16)]. Therefore, the full range of available system parameters are

$$\gamma, \beta, x_0, \theta_0 \quad \text{and} \quad (\varphi_{T1} \text{ or } \varphi_{T2} \text{ or } \alpha_{T1} \text{ or } \alpha_{T2}). \quad (17)$$

To perform inverse design, we can fix any of the four system parameters from Eq. (17) as design targets, leaving the fifth parameter free as our design parameter. We illustrate this process, setting the values of γ, β, x_0, and φ_{T1} as our design targets, which are outlined in Table II, and then calculating the θ_0 that achieves these desired kinematic configurations.

Before detailing the calculation of θ_0, we first justify our choice of design targets. We set $\gamma = 3\pi/4$ to simplify the kinematics, and $\beta = 10°$ to remain in the shaded

TABLE II. We can fix the four parameters γ, β, x_0, and φ_{T1} as design targets and show that there are two symmetric values of θ_0 that achieve these design targets. All units are in radians.

γ	β	x_0	φ_{T1}	$\theta_0(\gamma, \beta, x_0, \varphi_{T1})$
$3\pi/4$	$10°$	0.25	$\pi/2$	1.39
$3\pi/4$	$10°$	0.25	$\pi/2$	$2\pi - 1.39$

region of Fig. 3(c). We select φ as our design parameter over α since all of its facets are connected to standard origami linkages, so linking the units kinematically to an origami string [70], or an origami metamaterial [5] would be a simple task. We set $\varphi = \pi/2$ to further simplify analysis. We choose x_0 as the second design objective and keep it at a relatively low value of $1/4$ of the radius of the sphere, as limitations from the herein employed fabrication method imposes restrictions on manufacturing larger x_0 values. However, freer choice of manufacturing processes would allow for the selection of θ_0 as design target instead of parameter. Now we turn out attention to explicitly deriving the θ_0 required to achieve a given γ-β-$\varphi_{0,1}$-x_0 quartet. As detailed in SM A.8 [68], the spherical law of sines yields

$$\theta_0(x_0, \varphi_{0,1}) = 2\sin^{-1}\left(\frac{x_0}{2}\frac{\sqrt{A^2+1}}{A}\right) \quad (18a)$$

or

$$2\pi - 2\sin^{-1}\left(\frac{x_0}{2}\frac{\sqrt{A^2+1}}{A}\right), \quad (18b)$$

where

$$A = \frac{\sin\eta}{\frac{2}{x_0}\sin\frac{\varphi_{0,1}}{2}\sin\gamma - \cos\eta}. \quad (19)$$

Notice that Eq. (18) reveals there are two possible θ_0 values that satisfy our desired $\varphi_{0,1}$ and x_0, where the first applies for $\theta_0 \in (0, \pi)$ and the second for $\theta_0 \in (\pi, 2\pi)$. This is summarized in Table II.

To understand the physical difference between these two values of θ_0, we choose a representative design point of $\varphi_{0,1} = \pi/2$ and $x = 0.25$ for simplicity. Using Eq. (18a) we obtain the value $\theta_0 = 1.39$, and using Eq. (18b) we obtain the value $\theta_0 = 2\pi - 1.39$, both of which satisfy our design requirement. Figure 7(a) shows what the stable states and the folding pathways look like for $\theta_0 = 1.39$. Recall that $\theta_0 = 1.39$ and $x = 0.25$ were the parameters used in the preceding kinematic analysis, and that stable states, T1, T2, and T3, were indeed at $\varphi = \pi/2$, $\varphi = 3\pi/2$ and $\varphi = \pi$, as shown in Fig. 5(c), showcasing the predictive power of the inverse design. Figure 7(b) demonstrates the impact of the alternative choice of $\theta_0 = 2\pi - 1.39$. Notice that T1 and T2 switch are now located on the right-hand path, while T3 now lies on the left-hand path. From this, we can conclude that if $\theta_0 \in (0, \pi)$ [Eq. (18a)] then the two symmetric stable states will have $\alpha \in (0, \pi)$, whereas if we chose the $\theta_0 \in (\pi, 2\pi)$ [Eq. (18b)] we will have that the two symmetric stable states have $\alpha \in (\pi, 2\pi)$.

IX. CONCLUSION

We show via analysis and experiments a simplified technique of modeling Miura-Ori units with stretchable creases. Our analysis is based on a tractable model enabling the closed-form prediction of the stable state and folding paths of four-vertex, non-Euclidean origami units with crease stretching. The derived model can accurately predict almost all of the observed behavior of a physical system. The model also

enables an inverse design technique that gives two symmetric solutions for a desired shape. In theoretical terms, this is accomplished by connecting the disconnected regimes of non-Euclidean origami via crease stretching. This work provides an analytical model to access the design space of multistable origami, and lays the framework to allow for efficient inverse design of desired shapes based on accessible closed-form solutions, the stability of which does not require actuation systems or facet deformation.

[1] D. Melancon, A. E. Forte, L. M. Kamp, B. Gorissen, and K. Bertoldi, Adv. Funct. Mater. **32**, 2201891 (2022).

[2] P. Bhovad and S. Li, Sci. Rep. **11**, 13002 (2021).

[3] E. Hawkes, B. An, N. M. Benbernou, H. Tanaka, S. Kim, E. D. Demaine, D. Rus, and R. J. Wood, Proc. Natl. Acad. Sci. USA **107**, 12441 (2010).

[4] S. Felton, M. Tolley, E. Demaine, D. Rus, and R. Wood, Science **345**, 644 (2014).

[5] M. Schenk and S. D. Guest, Proc. Natl. Acad. Sci. USA **110**, 3276 (2013).

[6] E. T. Filipov, T. Tachi, and G. H. Paulino, Proc. Natl. Acad. Sci. USA **112**, 12321 (2015).

[7] D.-Y. Lee, S.-R. Kim, J.-S. Kim, J.-J. Park, and K.-J. Cho, Soft Robot. **4**, 163 (2017).

[8] L. H. Dudte, G. P. Choi, and L. Mahadevan, Proc. Natl. Acad. Sci. USA **118**, e2019241118 (2021).

[9] A. Walker and T. Stankovic, Commun. Mater. **3**, 4 (2022).

[10] Y. Zhao, Y. Wei, Y. Jia, S. Li, M. Zhang, L. Zeng, Y. Yang, and J. Mitani, J. Comput. Des. Eng. **9**, 1498 (2022).

[11] K. Xiao, Z. Liang, B. Zou, X. Zhou, and J. Ju, Nat. Commun. **13**, 7474 (2022).

[12] C. D. Santangelo, Soft Matter **16**, 94 (2020).

[13] S. J. Callens and A. A. Zadpoor, Mater. Today **21**, 241 (2018).

[14] V. Brunck, F. Lechenault, A. Reid, and M. Adda-Bedia, Phys. Rev. E **93**, 033005 (2016).

[15] E. A. Peraza-Hernandez, D. J. Hartl, R. J. Malak Jr., and D. C. Lagoudas, Smart Mater. Struct. **23**, 094001 (2014).

[16] J. L. Silverberg, J.-H. Na, A. A. Evans, B. Liu, T. C. Hull, C. D. Santangelo, R. J. Lang, R. C. Hayward, and I. Cohen, Nat. Mater. **14**, 389 (2015).

[17] C. Liu and S. M. Felton, Phys. Rev. Lett. **121**, 254101 (2018).

[18] K. Liu, T. Tachi, and G. H. Paulino, Nat. Commun. **10**, 4238 (2019).

[19] S.-M. Baek, S. Yim, S.-H. Chae, D.-Y. Lee, and K.-J. Cho, Sci. Rob. **5**, eaaz6262 (2020).

[20] B. H. Hanna, J. M. Lund, R. J. Lang, S. P. Magleby, and L. L. Howell, Smart Mater. Struct. **23**, 094009 (2014).

[21] B. Sargent, J. Butler, K. Seymour, D. Bailey, B. Jensen, S. Magleby, and L. Howell, J. Mech. Rob. **12**, 041005 (2020).

[22] H. Fang, S. Li, H. Ji, and K. W. Wang, Phys. Rev. E **95**, 052211 (2017).

[23] S. Waitukaitis, R. Menaut, Bryan Gin-ge Chen, and M. van Hecke, Phys. Rev. Lett. **114**, 055503 (2015).

[24] Bryan Gin-ge Chen and C. D. Santangelo, Phys. Rev. X **8**, 011034 (2018).

[25] S. Waitukaitis and M. van Hecke, Phys. Rev. E **93**, 023003 (2016).

[26] M. Stern, V. Jayaram, and A. Murugan, Nat. Commun. **9**, 4303 (2018).

[27] T. Tachi and T. C. Hull, J. Mech. Rob. **9**, 021008 (2017).

[28] M. Berry, M. E. Lee-Trimble, and C. D. Santangelo, Phys. Rev. E **101**, 043003 (2020).

[29] S. Waitukaitis, P. Dieleman, and M. van Hecke, Phys. Rev. E **102**, 031001(R) (2020).

[30] K. A. Seffen, Phys. Rev. E **94**, 013002 (2016).

[31] J. McInerney, B. G. Chen, L. Theran, C. D. Santangelo, and D. Z. Rocklin, Proc. Natl. Acad. Sci. USA **117**, 30252 (2020).

[32] R. Foschi, T. C. Hull, and J. S. Ku, Phys. Rev. E **106**, 055001 (2022).

[33] K. Liu, P. P. Pratapa, D. Misseroni, T. Tachi, and G. H. Paulino, Adv. Mater. **34**, 2107998 (2022).

[34] K. Liu, T. Tachi, and G. H. Paulino, J. Appl. Mech. **88**, 091002 (2021).

[35] B. Liu, J. L. Silverberg, A. A. Evans, C. D. Santangelo, R. J. Lang, T. C. Hull, and I. Cohen, Nat. Phys. **14**, 811 (2018).

[36] L. Huang, P. Zeng, L. Yin, B. Liu, Y. Yang, and J. Huang, Mech. Mach. Theory **174**, 104886 (2022).

[37] F. Haas, Geometry and mechanics of hind-wing folding in Dermaptera and Coleoptera, Ph.D. thesis, Exeter University, Biological Sciences Department, 1994.

[38] H. Rajabi, N. Ghoroubi, K. Stamm, E. Appel, and S. Gorb, Acta Biomaterialia **60**, 330 (2017).

[39] A. M. Mountcastle and S. A. Combes, J. Exp. Biol. **217**, 1108 (2014).

[40] S. N. Gorb, Naturwissenschaften **86**, 552 (1999).

[41] Z. Song, Y. Yan, J. Tong, and J. Sun, J. Mater. Sci. **55**, 4524 (2020).

[42] F. Haas, S. Gorb, and R. Blickhan, Proc. R. Soc. London B **267**, 1375 (2000).

[43] K. Saito, S. Yamamoto, M. Maruyama, and Y. Okabe, Proc. Natl. Acad. Sci. USA **111**, 16349 (2014).

[44] F. Haas, S. Gorb, and R. Wootton, Arthropod Struct. Dev. **29**, 137 (2000).

[45] J. A. Faber, A. F. Arrieta, and A. R. Studart, Science **359**, 1386 (2018).

[46] T. Jules, F. Lechenault, and M. Adda-Bedia, Soft Matter **15**, 1619 (2019).

[47] T. Jules, F. Lechenault, and M. Adda-Bedia, Phys. Rev. E **102**, 033005 (2020).

[48] B. Y. Dharmadasa and F. Lopez Jimenez, *Proceedings of the AIAA Scitech Forum* (AIAA, Reston, VA, 2021), p. 1258.

[49] M. Gori and F. Bosi, Extreme Mech. Lett. **56**, 101849 (2022).

[50] A. Iniguez-Rabago and J. T. Overvelde, Extreme Mech. Lett. **56**, 101881 (2022).

[51] C. Huang, T. Tan, X. Hu, F. Yang, and Z. Yan, Appl. Phys. Lett. **121**, 051902 (2022).

[52] M. E. Lee-Trimble, J.-H. Kang, R. C. Hayward, and C. D. Santangelo, Soft Matter **18**, 6384 (2022).

[53] H. Zhang, H. Feng, J.-L. Huang, and J. Paik, Extreme Mech. Lett. **45**, 101213 (2021).

[54] Y. Feng, M. Wang, and X. Qiu, Int. J. Solids Struct. **241**, 111530 (2022).

[55] P. Zhao, J. Liu, C. Wu, S. Ye, Q. Yang, and G. Hao, Int. J. Mech. Sci. **255**, 108444 (2023).

[56] M. G. Walker and K. A. Seffen, Thin-Walled Struct. **124**, 538 (2018).

[57] W. Kim, J. Byun, J.-K. Kim, W.-Y. Choi, K. Jakobsen, J. Jakobsen, D.-Y. Lee, and K.-J. Cho, Sci. Rob. **4**, eaay3493 (2019).

[58] H. Rajabi, S. H. Eraghi, A. Khaheshi, A. Toofani, C. Hunt, and R. J. Wootton, Proc. Natl. Acad. Sci. USA **119**, e2211861119 (2022).

[59] S. Daynes, R. S. Trask, and P. M. Weaver, Smart Mater. Struct. **23**, 125011 (2014).

[60] S. Mintchev, J. Shintake, and D. Floreano, Sci. Rob. **3**, eaau0275 (2018).

[61] F. Lechenault and M. Adda-Bedia, Phys. Rev. Lett. **115**, 235501 (2015).

[62] T. Yu, Int. J. Solids Struct. **246-247**, 111588 (2022).

[63] M. G. Walker, Phys. Rev. E **101**, 043001 (2020).

[64] S. Rojas, D. M. Boston, and A. F. Arrieta, *Bioinspiration, Biomimetics, and Bioreplication IX* (SPIE, Belingham, WA, 2019), Vol. 10965, pp. 134–142.

[65] S. Rojas, K. S. Riley, and A. F. Arrieta, J. R. Soc. Interface. **19**, 20220426 (2022).

[66] M. Koryo, Inst. Space Astronaut. Sci. Rep. **618**, 1 (1985).

[67] I. Todhunter, *Spherical Trigonometry, for the Use of Colleges and Schools: With Numerous Examples* (Macmillan, 1863).

[68] See Supplemental Material at http://link.aps.org/supplemental/10.1103/PhysRevE.108.055001 for a detailed description of the kinematics of the spherical trigonometry and the Lagrangian energetic analysis.

[69] Y. Li and S. Pellegrino, J. Mech. Phys. Solids **136**, 103772 (2020).

[70] S. Kamrava, D. Mousanezhad, S. M. Felton, and A. Vaziri, Adv. Mater. Technol. **3**, 1700276 (2018).